

# **Determination of the beam asymmetry $\Sigma$ in $\eta$ - and $\eta'$ -photoproduction using Bayesian statistics**

JAKOB MICHAEL KRAUSE

Masterarbeit in Physik  
angefertigt im Helmholtz-Institut für Strahlen- und  
Kernphysik

vorgelegt der  
Mathematisch-Naturwissenschaftlichen Fakultät  
der  
Rheinischen Friedrich-Wilhelms-Universität  
Bonn

Sep 2022

DRAFT

I hereby declare that this thesis was formulated by myself and that no sources or tools other than those cited were used.

Bonn, .....  
Date

.....  
Signature

- 1. Gutachterin: JUN. PROF. DR. ANNIKA THIEL
- 2. Gutachter: PROF. DR. JOCHEN DINGFELDER

DRAFT

# Contents

---

<b>1</b>	<b>Introduction</b>	<b>1</b>
1.1	Photoproduction of Pseudoscalar Mesons . . . . .	4
1.2	Measurement of Polarization Observables . . . . .	5
1.3	Introduction to BAYESIAN statistics . . . . .	5
1.4	Motivation and Structure of this Thesis . . . . .	5
<b>2</b>	<b>Experimental Setup</b>	<b>7</b>
2.1	Production of (polarized) high energy photon beam . . . . .	7
2.1.1	Tagger . . . . .	8
2.2	Beam Target . . . . .	8
2.3	Calorimeters . . . . .	8
2.4	Trigger . . . . .	8
<b>3</b>	<b>Event selection</b>	<b>11</b>
3.1	Preselection and charge cut . . . . .	11
3.2	Time of particles . . . . .	12
3.3	Kinematic constraints . . . . .	14
3.3.1	Derivation of cut conditions . . . . .	14
3.3.2	Determination of cut ranges . . . . .	15
3.3.3	Quality of event selection . . . . .	21
3.4	Investigation of background and additional cuts . . . . .	22
3.4.1	Inspecting plausibility of background reactions . . . . .	22
3.4.2	Misidentification of background reactions . . . . .	25
3.4.3	Examination of additional cuts . . . . .	28
<b>4</b>	<b>Determination of the beam asymmetry <math>\Sigma_\eta</math></b>	<b>15</b>
4.1	BAYESIAN fit to event yield asymmetries . . . . .	15
4.1.1	Application of method to toy Monte Carlo data . . . . .	15
4.1.2	Application of method to real data . . . . .	15
4.2	Event based fit . . . . .	15
4.2.1	Application of method to toy Monte Carlo data . . . . .	15
4.2.2	Application of method to real data . . . . .	15
4.3	Discussion . . . . .	15
<b>6</b>	<b>Summary and outlook</b>	<b>19</b>
<b>A</b>	<b>Useful information</b>	<b>21</b>

<b>Bibliography</b>	<b>23</b>
<b>List of Figures</b>	<b>25</b>
<b>List of Tables</b>	<b>27</b>

DRAFT

## Event selection

The determination of polarization observables needs to be completed for particular reactions (cf. chapter 1), such as the photoproduction of e.g. a single  $\eta'$  meson. However, the recorded events contain data from the decay products of all possible final states in addition to combinatorical background. Thus, event candidates for the desired reaction have to be extracted before they are considered for further analysis. Table 3.1 shows the five most probable decay modes of the  $\eta'$  meson. Three of these result in final states which only contain photons and are thus reliably measurable with the CBELSA/TAPS experiment. Only the  $\eta' \rightarrow \gamma\gamma$  decay channel was considered for further analysis; the  $\omega\gamma$  channel provides negligible statistics and considering the acceptance of detecting six photons in the final state, the expected yield of the  $\eta' \rightarrow \gamma\gamma$  decays should be roughly equal to the  $\eta' \rightarrow \pi^0\pi^0\eta \rightarrow 6\gamma$  final state [Afz22]. Offering a cleaner, three-particle final state, the  $\eta' \rightarrow \gamma\gamma$  channel was then favored in the course of this thesis.

Decay mode		Branching ratio
$\pi^+\pi^-\eta$		42.6%
$\rho^0\gamma$	$\rightarrow \pi^+\pi^-\gamma$	28.9% (28.9%)
$\pi^0\pi^0\eta$	$\rightarrow 6\gamma$	22.8% (8.8%)
$\omega\gamma$	$\rightarrow \pi^+\pi^-\pi^0\gamma/\pi^0\gamma\gamma$	2.52% (2.2%/0.21%)
$\gamma\gamma$		2.3%

**Table 3.1:** The five most probable decay modes of the  $\eta'$  meson. The most probable further decay with according branching ratio is shown in brackets.[Zyl+20]

The process of *event selection* for the reaction  $\gamma p \rightarrow p\eta' \rightarrow p\gamma\gamma$  is outlined in the following chapter. Note that in this thesis the analysis of data from  $\eta$ -photoproduction starts with this process already completed, which is described in detail in reference [Afz19].

### 3.1 Preselection and charge cut

Since the polarization degree can only be evaluated reliably up to 1 800 MeV and the production threshold for  $\eta'$  mesons is  $E_\gamma = 1\,447$  MeV [Zyl+20], the beam photon energy range was restricted to 1 400 to 1 800 MeV from the very beginning. The measured events are then generally classified

depending on the number of particle energy deposits (PED). If the complete four-momenta of three final state particles are measured, they are referred to as 3PED events. Low energy protons however may either be only detected in the scintillators of the inner, forward or MiniTAPS detector – giving only directional information (2.5 PED) – or lost entirely (2 PED). Only 2.5PED and 3PED events were analyzed since the additional background contributions from 2PED events exceeded the additional signal contributions. It is worth noting that 3PED events are significantly dominant for  $\eta' \rightarrow \gamma\gamma$  reactions; the production threshold for  $\eta'$  mesons is so high energetic that the recoil proton will likely be detected. Figure 3.1 shows the distribution of the different event classes for  $\eta' \rightarrow \gamma\gamma$  production in MONTE CARLO data, with a clear preference towards 3PED events.

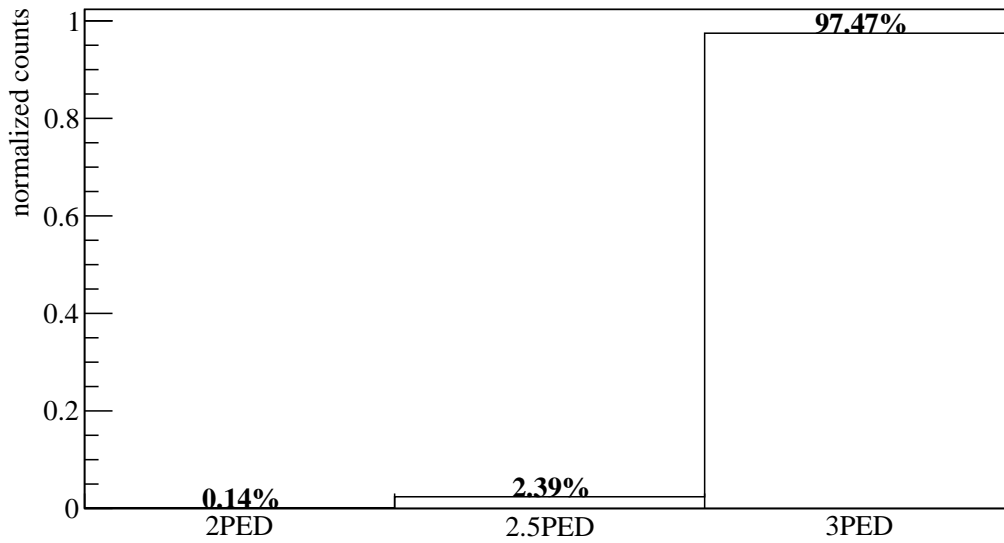


**Figure 3.1:** Distribution of event classes in  $\eta' \rightarrow \gamma\gamma$  production

To further improve the signal to background ratio, the charge information of the final state particles was utilized in the next step. In particular, to select  $\eta' \rightarrow \gamma\gamma$  reactions, one charged and two uncharged particles in the final state were demanded.

### 3.2 Time of particles

Due to its high count rate the tagging system (see section 2.1.1) will not only record beam photons which produce the detectable final state particles, but also several uncorrelated ones. To select only beam photons which will induce a photoproduction process the time information of the detected particles is used. It is shown in figure 3.2 for all particles involved in 2.5PED and 3PED events of  $\eta'$  photoproduction. In all cases prompt peaks centered around 0 ns (the trigger time) are visible. Since the final state photons move with velocity  $c$  their timing information does not underlie fluctuations, as is the case for the final state proton on the contrary. The tagged, uncorrelated beam photons are visible as flat background underneath the prompt peak in the time of the beam photon. Naturally, only coincident events may be referred to as  $\eta'$  candidates for the further analysis and thus only events

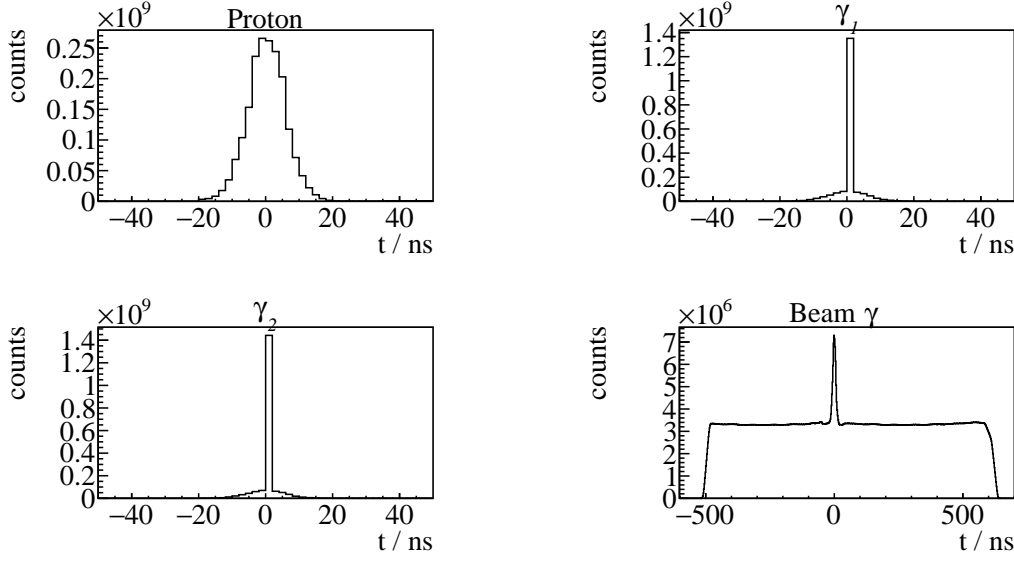


**Figure 3.2:** Time information of all final state particles and the beam photon for 3PED  $\eta'$  production

with time information of at least one final state particle are kept. Photons need to be detected in the MiniTAPS or forward detector to acquire time information. To determine coincidence it is convenient to define the *reaction time*

$$t_{\text{reaction}} = \begin{cases} t_{\text{beam}} - t_{\text{meson}} & \text{meson time exists} \\ t_{\text{beam}} - t_{\text{recoil}} & \text{meson time does not exist,} \end{cases} \quad (3.1)$$

where the meson time  $t_{\text{meson}}$  is appointed either the averaged time of both decay photons or the time of a single photon if only one photon has time information.  $t_{\text{beam}}$  and  $t_{\text{recoil}}$  are the time of the beam photon and recoil proton, respectively. Figure 3.3 shows the reaction time for 2.5PED and 3PED events; a clear prompt peak centred at 0 is visible, the colored area indicates the chosen range of  $t_{\text{reaction}} \in [-8, 5]\text{ns}$ . However, this cut still contains random time background underneath the prompt peak. This may be accounted for by *sideband subtraction*, assuming the background is flat. All events residing in the prompt peak with  $t_r \in [-8, 5]\text{ns}$  will be assigned a weight of  $w_p = +1$  while sideband events with  $t_r \in [-200, -100]\text{ns} \vee t_r \in [100, 200]\text{ns}$  will be assigned a weight of  $w_s = -\frac{13}{200}$ . Any histogram  $N$  that is filled in the following will then consist of prompt peak events  $N_{\text{prompt}}$  and sideband events  $N_{\text{sideband}}$

$$N = N_{\text{prompt}} + w_s \cdot N_{\text{sideband}},$$

such that the random time background underneath the prompt peak is subtracted. In addition, the time difference between meson and proton and between the two photons is demanded to be within  $[-10, 10]\text{ns}$ . All described cuts to the data, including the sideband subtraction are referred to as the *time cut* in the following.



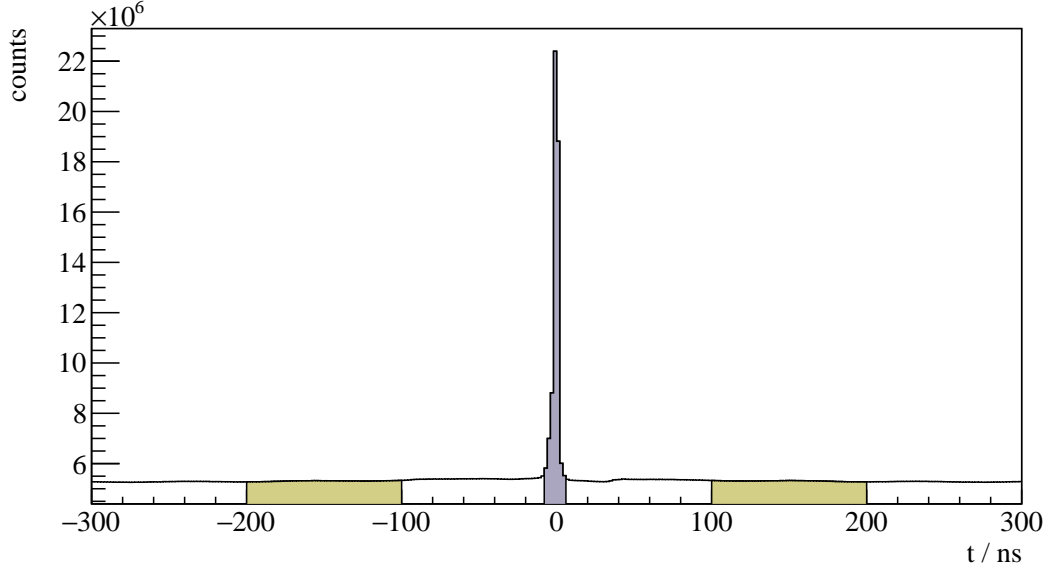


**Figure 3.3:** Reaction time  $t_r$  for 3PED  $\eta'$  production

### 3.3 Kinematic constraints

Up until now mainly combinatorial background was discussed. However one can derive kinematical constraints from energy and momentum conservation to exclusively select the desired reaction. The derivation is discussed first, followed by the determination of the derived cut conditions.

#### 3.3.1 Derivation of cut conditions

Let  $p_{\text{beam}}$  and  $p_p$  be the four momenta of the initial state beam photon and proton, respectively. Then

$$p_{\text{beam}} + p_p = p_{\text{recoil}} + p_{\text{meson}} \quad (3.2)$$

holds, with  $p_{\text{recoil}}$  being the momentum of the recoiling proton and  $p_{\text{meson}}$  the meson momentum.

#### Coplanarity

In the initial state there is vanishing transversal momentum  $p_{xy}$  since the target protons are at rest and the beam photon impinges in  $z$ -direction. Naturally, this transversal momentum has to vanish in the final state as well, such that

$$\mathcal{P}_{xy} [p_{\text{recoil}} + p_{\text{meson}}] = 0, \quad (3.3)$$

where  $\mathcal{P}_{xy}$  is the projection operator to the transversal plane. Equation (3.3) is valid if and only if meson and proton lie back to back (coplanar) in the  $x$ - $y$  plane, which is quantified by the difference of their azimuthal angles  $\phi_{\text{meson}}$  and  $\phi_{\text{recoil}}$  being  $180^\circ$  in the laboratory-frame

$$\Delta\phi := \phi_{\text{meson}}^{\text{LAB}} - \phi_{\text{recoil}}^{\text{LAB}} \stackrel{!}{=} 180^\circ. \quad (3.4)$$

### Polar angle difference

If all initial and final state momenta are measured, the reaction described by equation (3.2) is *overdetermined*, such that one final state particle can be treated as a "missing particle"  $X$  with momentum  $p_X$ :

$$p_X = p_{\text{beam}} + p_p - p_{\text{meson}}. \quad (3.5)$$

One can then use

$$\Delta\theta := \theta_{p_X}^{\text{LAB}} - \theta_{p_{\text{recoil}}}^{\text{LAB}} \stackrel{!}{=} 0 \quad (3.6)$$

as a further constraint to the data.

### Missing mass

The previously described angular cuts are only applicable if all final state particles have been detected. Independently of the detection of the recoil proton the mass of the missing particle  $m_X^2 = p_X^2$  can be determined and compared with the proton mass of  $m_p = 938.27 \text{ MeV}$  [Zyl+20]. From equation (3.5) it follows that

$$m_X = \sqrt{(E_\gamma + m_p - E_{\text{meson}})^2 - p_{x,\text{meson}}^2 - p_{y,\text{meson}}^2 - (E_\gamma - p_{z,\text{meson}})^2}. \quad (3.7)$$

### Invariant mass

The measurement of the invariant mass of the two final state photons does also not require the measurement of the recoil proton. The knowledge of both four-momenta suffices, since

$$m_{\text{meson}} = \sqrt{p_{\text{meson}}^2} = \sqrt{(p_{\gamma_1} + p_{\gamma_2})^2} = \sqrt{2E_{\gamma_1}E_{\gamma_2}(1 - \cos \alpha_{\gamma_1\gamma_2})}, \quad (3.8)$$

where  $E_{\gamma_i}$  are the measured photon energies and  $\alpha_{\gamma_1\gamma_2}$  is the angle spanned by the two photon momenta. To select only  $\eta'$  candidates  $m_{\text{meson}} = m_{\eta'} = 957.78 \text{ MeV}$  is demanded. Remarkably, the cut on the invariant mass of the final state photons is the only one to uniquely select  $\eta'$  production candidates so far. All other cuts apply similarly to arbitrary meson photoproduction.

### 3.3.2 Determination of cut ranges

The constraints described in the previous section must not be understood as strict equalities, cf. equations (3.3),(3.6),(3.7) and (3.8). The quantities of interest will rather describe distributions around the desired value, such that confidence intervals may be extracted by fitting to said distributions. This is done iteratively:

Let  $C_I^\chi$  be the cut operator that restrains the data  $\mathcal{D}$  such that the (generic) cut variable

$$\chi \in \{\Delta\theta, \Delta\phi, m_X, m_{\text{meson}}\}$$

lies in the interval  $\mathcal{I} \subseteq \mathbb{R}$ , such that

$$C_I^\chi : \mathcal{D} \mapsto \mathcal{D}_{\chi \in \mathcal{I}}. \quad (3.9)$$

After a first inspection of the data, initial guesses for the intervals  $\mathcal{I}, \mathcal{J}, \mathcal{K}, \mathcal{L}$  corresponding to the quantities  $\Delta\theta, \Delta\phi, m_X, m_{\text{meson}}$ , respectively, are made. Having established estimates for the cut ranges,

new ones are estimated by investigating the distribution of one cut variable obtained from the data while all other cut variables are constrained to the previously determined intervals. For example

$$\Delta\theta \left( C_{\mathcal{J}}^{\Delta\phi} C_{\mathcal{K}}^{m_x} C_{\mathcal{L}}^{m_{\text{meson}}} \mathcal{D} \right) \sim \text{normal}(\mu, \sigma),$$

where  $\mu \approx 0$ . This is done (with some adjustments to the fit function) for each cut variable. The parameters of the gaussian are determined from a  $\chi^2$  fit and used to assign new cut ranges. Simultaneously, Monte-Carlo (MC) data of relevant final states are fitted to match the measured values bin-wise. This is done on the one hand to check consistency between measured and MC data and on the other hand used to determine contributing background reactions. First, all mesonic final states that decay into two photons are considered, i.e.  $p\pi^0, p\eta, p\eta'$ , since the according peaks in the invariant mass spectrum will be visible. Also, a peak at the mass of the  $\omega$  (vector)-meson  $m_\omega$  will be visible; this stems from photoproduction reactions  $p\omega \rightarrow p\pi^0\gamma \rightarrow p3\gamma$  where one low energetic final state photon is lost, such that the reconstructed invariant mass still estimates the  $\omega$  mass. Further, one should investigate the impact of neutral final states, where some of the final state photons may get lost during reconstruction, as can be observed for  $p2\pi^0, p\pi^0\eta, p3\pi^0, p2\pi^0\eta$ <sup>1</sup> production. Lastly, possible misidentification of charged particles which then mimic a  $p\gamma\gamma$  final state are examined, such as  $p\pi^+\pi^-$  and  $n\pi^+$ . Table 3.2 lists all employed MC reactions and their respective final state particles, as well as a short explanation why the particular reaction was included in the fit.

Photoproduction reaction	Final state particles	Explanation
$p\pi^0$	$p\gamma\gamma$	prominent peak in the invariant mass spectrum
$p\eta$	$p\gamma\gamma$	
$p\omega$	$p\pi^0\gamma \rightarrow p3\gamma$	
$p\eta'$	$p\gamma\gamma$	
$p2\pi^0$	$p4\gamma$	lost photons cause a "3-particle" final state
$p\pi^0\eta$	$p4\gamma$	
$p3\pi^0$	$p6\gamma$	
$p2\pi^0\eta$	$p6\gamma$	
$p\pi^+\pi^-$		misidentification of charged particles
$n\pi^+$		

**Table 3.2:** Examined MC reactions that were used in sum for the fit

Since the invariant mass spectrum features rich contributions from many final states, it is difficult to describe by a (sum of) gaussian function(s), especially considering the background contributions. Thus, for the invariant mass the cut ranges are obtained from gaussian fits to the scaled MC data of the  $\eta'$  final state. Table 3.3 shows which fit function and cut range was used for each cut variable. In addition, it shows if the cut ranges were determined from MC or measured data. The newly obtained intervals  $\mathcal{I}', \mathcal{J}', \mathcal{K}', \mathcal{L}'$  serve again as input for the previous step. This is repeated until a certain convergence is reached, which is usually the case after a two or three iterations. Since the cut ranges may vary depending on beam energy and meson direction, they are determined in bins of the beam

<sup>1</sup> all mesons  $m$  decaying into two photons is implied:  $m \rightarrow \gamma\gamma\forall m$

cut variable	fit function	interval range	obtained from
$\Delta\theta$	GAUSS	$\mathcal{I}' = [\mu - 3\sigma, \mu + 3\sigma]$	data points
$\Delta\phi$	GAUSS	$\mathcal{J}' = [\mu - 3\sigma, \mu + 3\sigma]$	data points
$m_X$	NOVOSIBIRSK [Ike+00]	$\mathcal{K}' = [\mu - 2\sigma, \mu + 2\sigma]$	data points
$m_{\text{meson}}$	GAUSS	$\mathcal{L}' = [\mu - 2\sigma, \mu + 2\sigma]$	MC data

**Table 3.3:** Fit functions and cut ranges for each variable

energy and the polar angle of the meson in the center of mass system (CMS)

$$(E_\gamma, \cos \theta_{\eta'}^{\text{CMS}})^2.$$

Respecting the  $\eta'$  final state statistics, a binning of  $\Delta E_\gamma = 100$  MeV and  $\Delta \cos \theta = 1/3$  was chosen, spanning the energy range of 1 500 to 1 800 MeV. The theoretically accessible lower limit in the beam energy is provided by the production threshold of  $\eta'$  mesons at 1 447 MeV [Zyl+20]. Yet, the binning has to comply with the upper beam energy limit which is bounded from above<sup>3</sup> by the position of the coherent edge of the beamtime. It is given by 1 700 MeV and 1 800 MeV for the July/August and September/October beam times, respectively. If one were to include the production threshold into the analyzed range using the same binning, more background than  $\eta'$  events are collected from 1 400 to 1 500 MeV (see subsection 3.4.3), hence the chosen binning starts at 1 500 MeV.

### Coplanarity

Figure 3.4 shows the coplanarity spectra for the energy bin  $1\,500\text{ MeV} \leq E_\gamma < 1\,600\text{ MeV}$  and all angular bins. The data points are visualized by the open circles with error bars, while the black solid histogram is a fit of  $\eta' \rightarrow \gamma\gamma$  MC. As expected, a clear peak is visible at  $\Delta\phi = 180^\circ$ , which shows only slight dependence on beam energy and meson direction. A  $3\sigma$  interval obtained from a gaussian fit is indicated by the dashed red lines. Note that only MC spectra of the  $\eta'$  final state were fitted to the data since the coplanarity gives little reference points for a correct estimation of other final states that may contribute.

### Polar angle difference

Since the meson direction correlates with the detector(s) the final state photons hit, the polar angle difference depicts a clear directional dependence as can be seen in figure 3.5 for the energy bin  $1\,500\text{ MeV} \leq E_\gamma < 1\,600\text{ MeV}$  and all angular bins. In the CMS frame, meson and proton are emitted back to back. Thus, if the meson is emitted in backward direction ( $\cos \theta \sim -1$ ), the proton will be detected either in the forward or MiniTAPS detector, which have a better angular resolution than the Crystal Barrel calorimeter, leading to narrower distributions of  $\Delta\theta$ . The determined cut ranges are  $3\sigma$  intervals obtained from a gaussian fit to the data and are indicated by the red dashed lines. As before, no other than  $\eta'$  MC are fitted to the spectra.

<sup>2</sup> If not otherwise specified, from now on  $\cos \theta = \cos \theta_{\eta'}^{\text{CMS}}$

<sup>3</sup> Significantly beyond the coherent edge, the systematic error for the beam polarization degree gets too large ( $> 10\%$ )

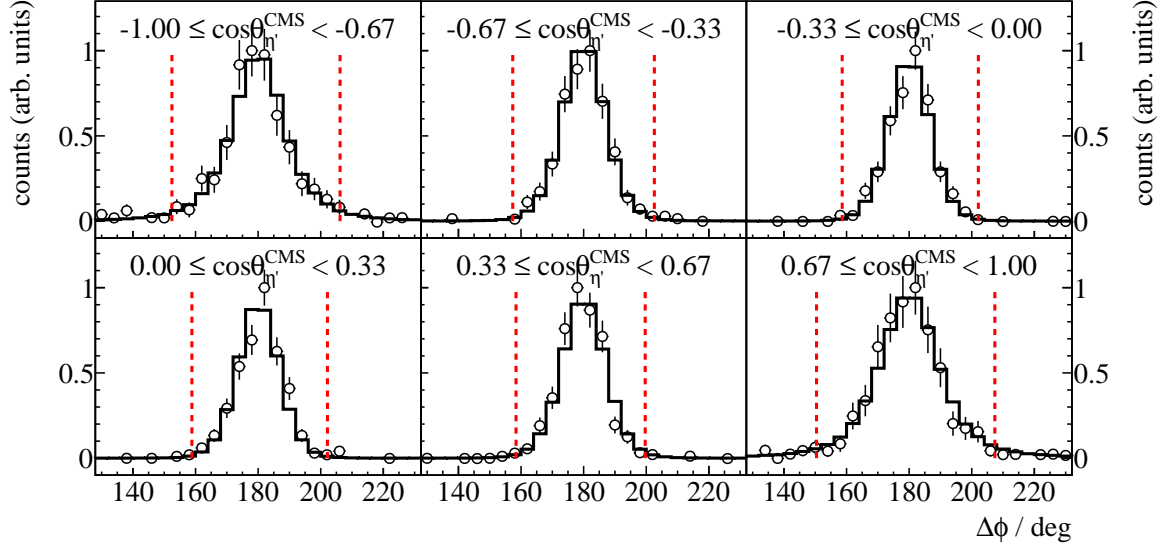


**Figure 3.4:** Coplanarity of the  $p\eta'$  final state with all other cuts applied for the energy bin  $1\,500\,\text{MeV} \leq E_\gamma < 1\,600\,\text{MeV}$ . The vertical dashed lines show the cut ranges obtained from a gaussian fit to the data (open circles). The solid black histograms represent fitted MC data of  $\eta' \rightarrow \gamma\gamma$

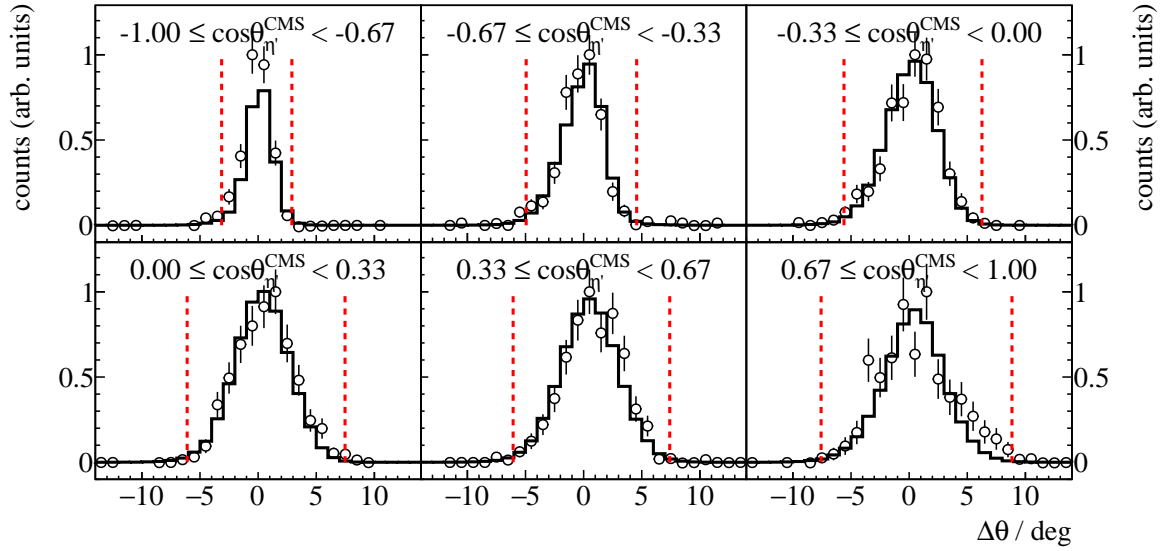


**Figure 3.5:** Polar angle difference of the  $p\eta'$  final state with all other cuts applied for the energy bin  $1\,500\,\text{MeV} \leq E_\gamma < 1\,600\,\text{MeV}$ . The vertical dashed lines show the cut ranges obtained from a gaussian fit to the data (open circles). The solid black histograms represent fitted MC data of  $\eta' \rightarrow \gamma\gamma$

### Missing mass

The missing mass spectra allow a first investigation of possible background reactions that pass event selection. For all angular bins of the first energy bin the missing mass is shown in figure 3.6; again, the open circles are the data points with corresponding statistical error bars. The solid colored histograms are fitted MC spectra of different possible background contributions while the black histogram is the signal contribution of  $\eta' \rightarrow \gamma\gamma$  photoproduction. The turquoise histogram is the sum of all MC histograms. Generally, most of the data can be described by the  $\eta'$  MC alone, but especially towards higher masses (and higher beam energies) background contributions extend the missing mass peak as flat background. These are reactions where the reconstructed meson mass  $m_{\text{meson}}^2 = E_{\text{meson}}^2 - \vec{p}_{\text{meson}}^2$  is smaller than the  $\eta'$  mass, resulting in larger values for the missing mass. Judging from the fit to the missing mass,  $2\pi^0$  and/or  $\pi^0\eta$  photoproduction may describe the background as both show similar shapes. All other previously mentioned reactions (table 3.2) do not contribute significantly. Better conclusions can be drawn from the invariant mass spectra as is discussed in the following section 3.4. The cut ranges for the missing mass are obtained from a Novosibirsk [Ike+00] fit to the data since the missing mass distribution is slightly asymmetric. However, since the tail parameter is small, still a symmetric cut of  $\pm 2\sigma$  was chosen. It was chosen narrower than the angular cuts to collect less background reactions.

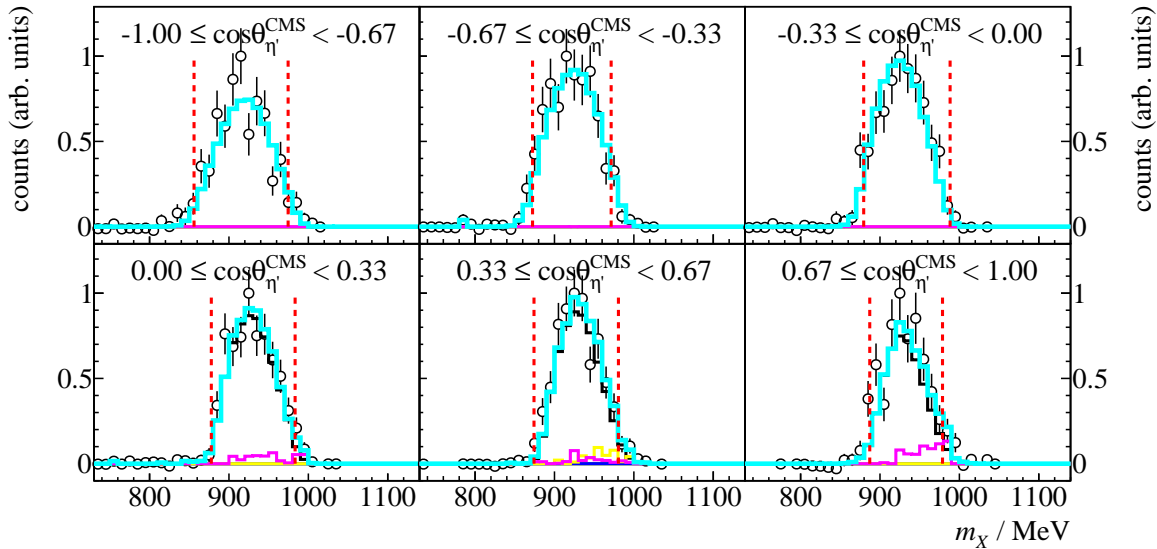


**Figure 3.6:** Missing mass of the  $p\eta'$  final state with all other cuts applied for the energy bin  $1\,500\,\text{MeV} \leq E_\gamma < 1\,600\,\text{MeV}$ . The vertical dashed lines show the cut ranges obtained from a fit to data (open circles) employing a Novosibirsk function. The solid colored histograms represent fitted MC data from relevant photoproduction reactions: in black  $\eta'$ , in green  $\pi^0$ , in red  $\eta$ , in blue  $\omega$ , in yellow  $2\pi^0$ , magenta  $\pi^0\eta$ . The turquoise histogram is the sum of all MC histograms.

### Invariant mass

Investigating the invariant mass spectrum of the final state photons allows to illustrate the impact of the event selection so far. As has been mentioned all cuts considered up to this point apply to arbitrary meson photoproduction. This means that the invariant mass spectrum will depict peaks belonging to mesons produced in the considered beam energy range. This is shown in figure 3.7 giving an overview over all energy and angular bins. All other cuts have been applied. The open circles represent data points and the different colored histograms MC data from relevant competing final states while the black histogram shows the signal contribution of  $\eta'$  MC. The turquoise histogram is the sum of all MC contributions and describes the data very well. It has again been found that no other than the shown final states contribute significantly or improve the description of data by MC spectra. As expected one can observe peaks belonging to  $\pi^0$ ,  $\eta$ ,  $\omega$  and  $\eta'$  photoproduction. A flat background underneath the complete spectrum is realized by  $2\pi^0$  and  $\pi^0\eta$  final state photons that have been wrongfully combined to two photons. Remarkably, the  $\pi^0$ ,  $\eta$  and  $\omega$  invariant mass distributions also depict long tails towards lower and higher masses, although they contribute only marginally to the sum of all MC spectra (note the logarithmic y-Scale). They can be explained by the fact that one low energetic photon is lost during reconstruction while the (high energetic) proton wrongfully creates two tracks of which one is then combined with the other photon as meson candidate [Afz19]. To finally select only  $\eta'$

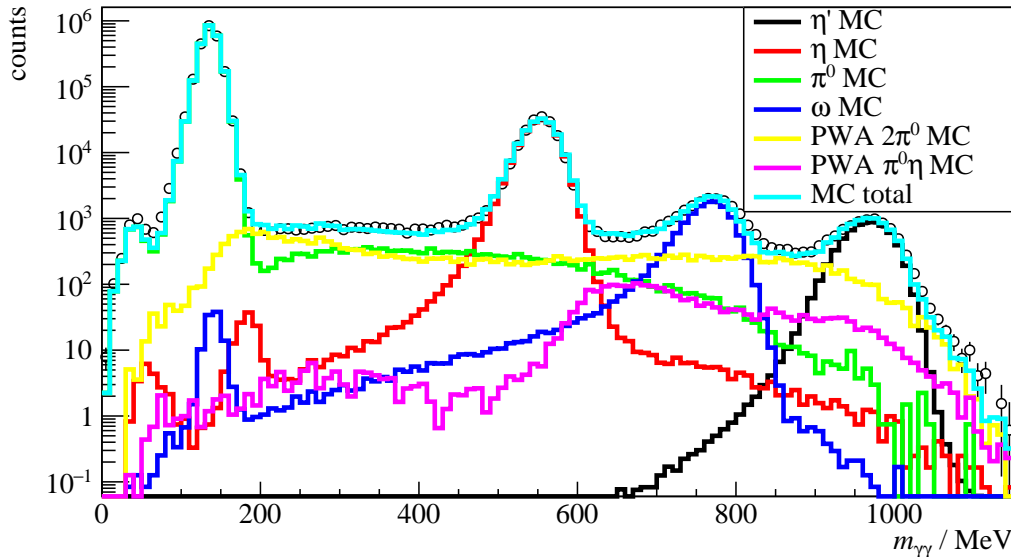


**Figure 3.7:** Invariant mass of the  $p\eta'$  final state with all other cuts applied for all energy and angular bins. The open circles represent the measured data, the solid colored histograms fitted MC data from relevant photoproduction reactions: in black  $\eta'$ , in green  $\pi^0$ , in red  $\eta$ , in blue  $\omega$ , in yellow  $2\pi^0$  and in magenta  $\pi^0\eta$ . The turquoise histogram is the sum of all MC histograms.

photoproduction event candidates the invariant mass cut is determined again in bins of beam energy and meson polar angle. This is shown in figure 3.8 for the first energy bin with all angular bins. Here, the same color coding as before applies, but the range of the invariant mass has been reduced to only cover the  $\eta'$  peak for visibility's sake. Additionally the cut ranges, representing a  $2\sigma$  interval obtained

from a gaussian fit to the  $\eta'$  MC, are shown as dashed, red lines. Considering the statistics the MC spectra still describe the data well. It is found again that the significant background contributions in the invariant mass range of interest are given by  $2\pi^0$  and  $\pi^0\eta$  photoproduction.

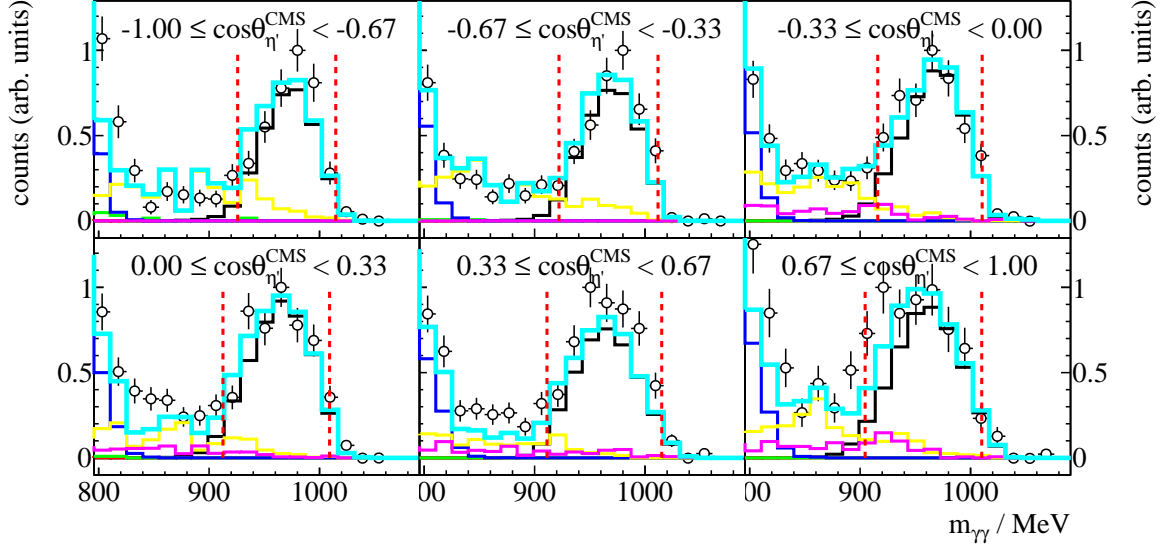


**Figure 3.8:** Invariant mass of the  $p\eta'$  final state with all other cuts applied for the energy bin  $1\,500\,\text{MeV} \leq E_\gamma < 1\,600\,\text{MeV}$ . The vertical dashed lines show the cut ranges obtained from a gaussian fit to the  $\eta'$  MC data (solid black histogram). The open circles represent the measured data, the solid colored histograms fitted MC data from relevant photoproduction reactions: in black  $\eta'$ , in green  $\pi^0$ , in red  $\eta$ , in blue  $\omega$ , in yellow  $2\pi^0$  and in magenta  $\pi^0\eta$ . The turquoise histogram is the sum of all MC histograms.

### 3.3.3 Quality of event selection

In order to investigate the impact of applied cuts the detector and analysis acceptance  $A(E_\gamma, \cos \theta)$  can be investigated. It is defined as the ratio of reconstructed events  $N^{\text{rec}}(E_\gamma, \cos \theta)$  to generated events  $N^{\text{gen}}(E_\gamma, \cos \theta)$

$$A := \frac{N^{\text{rec}}(E_\gamma, \cos \theta)}{N^{\text{gen}}(E_\gamma, \cos \theta)} \quad (3.10)$$

and is shown in figure 3.9. Acceptance holes are visible in very forward and in backward direction which can be contributed to events where the proton escapes the calorimeters or is absorbed in insensitive material. Also, events close to threshold are unlikely to be reconstructed which can also be explained by low energy protons and/or low energy photons. A maximum acceptance of  $\tilde{A} \approx 0.61$  is reached which can be understood considering the cuts that have been made; each  $3\sigma$  cuts retains 99% of events and each  $2\sigma$  cut 95%. Assuming detection efficiencies of 90% for the two uncharged photons and 85% for the charged proton ([hartmannphd; Afz19]) it is evident that  $0.99^2 \cdot 0.95^2 \cdot 0.9^2 \cdot 0.85 \approx 0.61$ . In total,  $8 \cdot 10^3$   $\eta'$  events were extracted which nonetheless still contain background contaminations. In order to take this into account in the later analysis the fraction



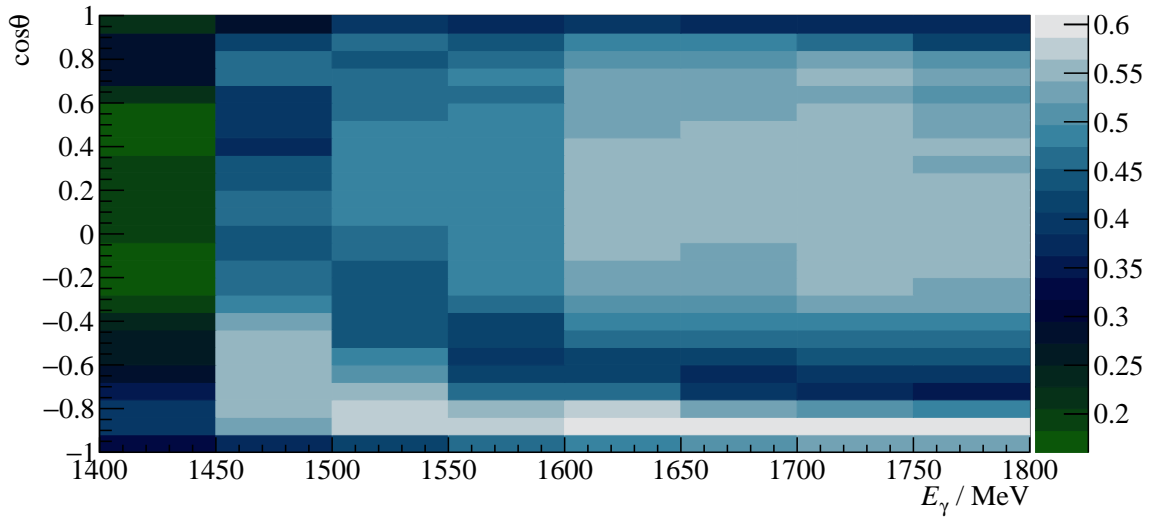


**Figure 3.9:** Acceptance for the reaction  $\gamma p \rightarrow p \eta'$  after all cuts that have been discussed so far for 2.5PED and 3PED events

of background is determined for each bin in beam energy and meson polar angle. It is estimated as the fraction of background MC events to total MC events and shown in figure 3.10. For most bins around 15% of all events are misidentified as  $\eta'$  events. Especially at very forward  $\cos \theta \rightarrow 1$  and backward  $\cos \theta \rightarrow -1$  angles the background contributions are significantly higher, reaching up to 45%.

### 3.4 Investigation of background and additional cuts

So far the background reactions in the  $\eta'$  cut ranges have been discussed only phenomenologically as they describe the measured invariant mass spectra best. In the following the plausibility and causality of these background contributions shall be discussed. Furthermore it is investigated if the found background contributions may be reduced or eliminated by additional cut conditions.

#### 3.4.1 Inspecting plausibility of background reactions

To evaluate the likelihood that the background contributions are made up of  $2\pi^0$  or  $\pi^0\eta$  production events the respective production cross sections in the inspected beam energy region and branching ratios (BR) to purely photonic final states are examined, see table 3.4. Also displayed is the maximum acceptance  $\tilde{A}$  which is additionally shown in figure 3.11. Both possible background reactions exceed  $\eta'$  photoproduction in cross section and also in relative frequency of purely photonic final states. At the same time the acceptance is almost vanishing, proving that the kinematic cuts are generally very effective.

Since the total number of events is proportional to the cross section  $\sigma$ , branching ratio BR and

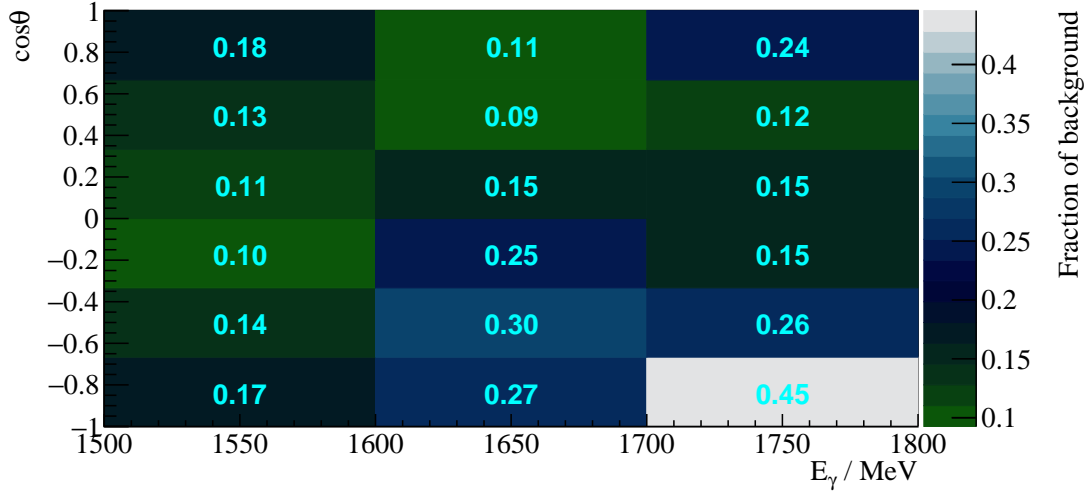


**Figure 3.10:** Fraction of background events in the analyzed beam energy and angular bins.

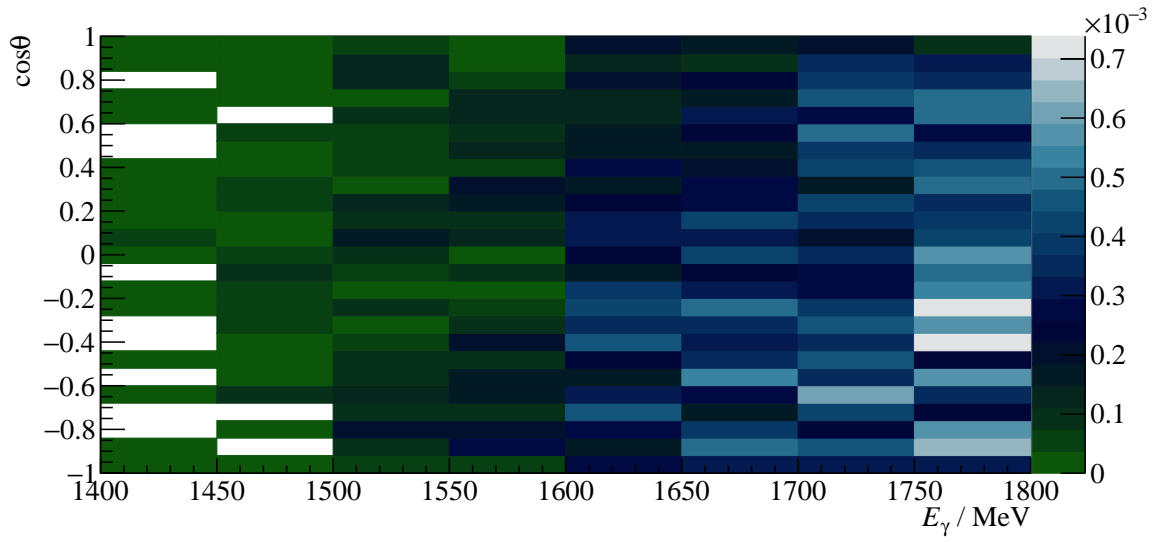
reaction	$\sigma / \mu\text{b}$	BR to $n\gamma$	$\tilde{A}$
$\gamma p \rightarrow p\eta'$	$\approx 1$ [Cre+09]	0.02	0.61
$\gamma p \rightarrow p2\pi^0$	$\lesssim 5$ [Die+20]	$0.98^2 = 0.96$	$7 \cdot 10^{-4}$
$\gamma p \rightarrow p\pi^0\eta$	$\approx 3$ [Käs+18]	$0.98 \cdot 0.38 = 0.37$	$2 \cdot 10^{-4}$

**Table 3.4:** Total cross sections  $\sigma$  in the energy range 1 500 to 1 800 MeV, branching ratios (BR) to  $n\gamma$  final states and maximum acceptance  $\tilde{A}$  for signal and possible background contributions

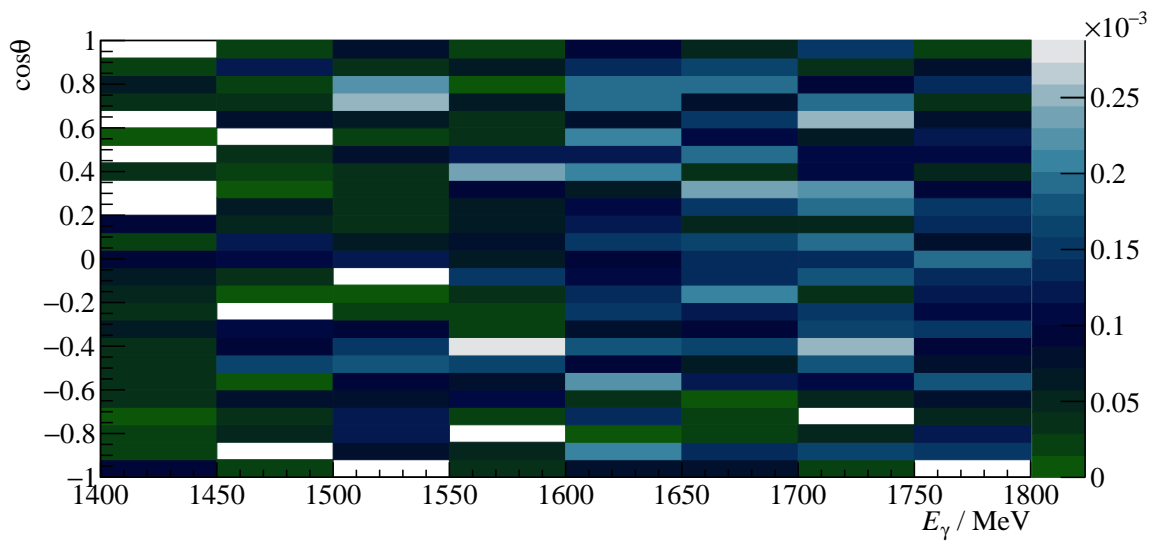
acceptance  $\tilde{A}$ , the ratio of reconstructed background to signal events is then given by

$$R = \frac{\sigma \cdot \text{BR} \cdot \tilde{A}}{\sigma_{\eta'} \cdot \text{BR}_{\eta' \rightarrow \gamma\gamma} \cdot \tilde{A}_{\eta'}} = \frac{\sigma \cdot \text{BR} \cdot \tilde{A}}{1 \mu\text{b} \cdot 0.02 \cdot 0.61}.$$

One finds  $R \lesssim 0.3$  and  $R \lesssim 0.05$  for  $2\pi^0$  and  $\pi^0\eta$  photoproduction, respectively. Although less than 0.1% of two meson production reactions are misidentified as  $\eta'$  events they make up a significant portion of background in  $\eta'$  data, as considering the according branching ratios and cross sections showed. Furthermore, the previous empirical assumption to only include  $2\pi^0$  and  $\pi^0\eta$  MC in the fit to describe the data is now justified since the found background percentages agree well with the now motivated upper boundaries.



(a)  $\gamma p \rightarrow p 2\pi^0$



(b)  $\gamma p \rightarrow p \pi^0 \eta$

**Figure 3.11:** Acceptance for possible background contributions

### 3.4.2 Misidentification of background reactions

It has been reasonably established that the main background reactions that escape the  $\eta'$  event selection cuts are realized by  $2\pi^0$  and  $\pi^0\eta$  production. However, it remains to explain why a four-photon final state is misidentified as  $\eta'$  event. In order to do so the MC simulations of the respective final states were investigated. One observes that for those events that passed the  $\eta'$  cuts the generated photon energies for two photons often were of order  $E_{\gamma,i} \sim \mathcal{O}(10 \text{ MeV})$  and the other two of order  $E_{\gamma,i} \sim \mathcal{O}(100 \text{ MeV})$ . The reconstructed energies however only displayed energies of order  $E_{\gamma,i} \sim \mathcal{O}(100 \text{ MeV})$ . During the reconstruction of final state four momenta, a minimum energy of 20 MeV per cluster is demanded in order to suppress electromagnetic background. This threshold is not passed or only closely passed by both lowest energy final state photons of  $2\pi^0$  production for  $\sim 60\%$  of all events, see figure 3.12. Similarly,  $\sim 70\%$  of  $\pi^0\eta$  events have a final state photon which does not or only closely pass

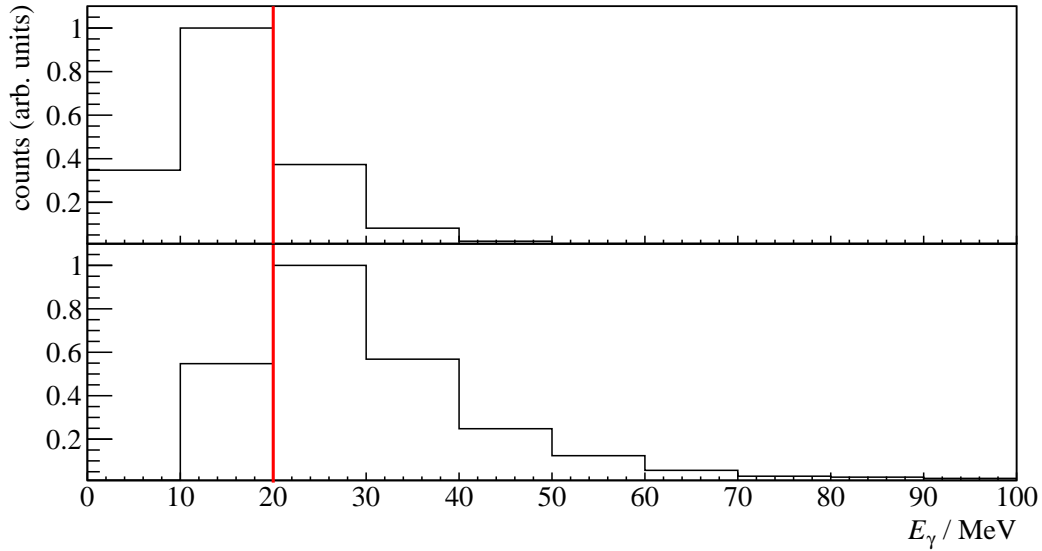


**Figure 3.12:** Generated energies of the two lowest energy photons in  $2\pi^0$  photoproduction MC data. The threshold of 20 MeV is marked by a vertical red line. Lowest energy photon is shown on the top, second lowest energy photon is shown on the bottom.

the threshold of 20 MeV. Other than in  $2\pi^0$  reactions, this does only apply for one of the lowest energy photons while the other significantly exceeds the threshold of 20 MeV, see figure 3.13. Those photons with an energy above threshold may still be lost during reconstruction because they are falsely combined to one cluster with one of the two highest energy photons as a investigation of photon directions revealed; figure 3.14 shows the polar angle difference between the second lowest energy photon and the second highest energy photon of the MC  $\pi^0\eta$  final state which clearly peaks centered at 0. Similar results are found with  $2\pi^0$  production events. It is evident that neither the two lost photons, nor the two reconstructed photons are correlated, i.e. decay products of the same meson.

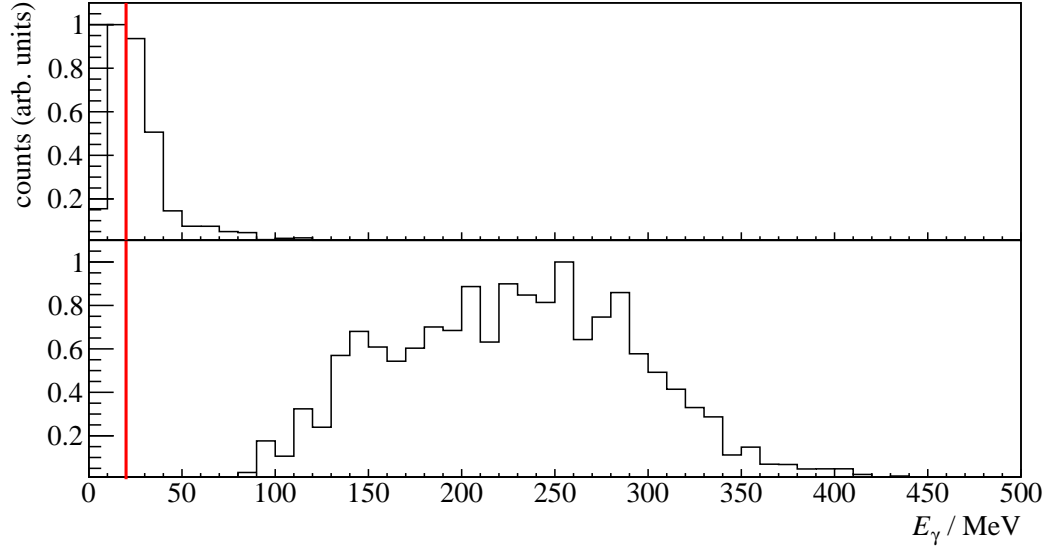


**Figure 3.13:** Generated energies of the two lowest energy photons in  $2\pi^0$  and  $\pi^0\eta$  photoproduction MC data. The threshold of 20 MeV is marked by a vertical red line. Lowest energy photon is shown on the top, second lowest energy photon is shown on the bottom.

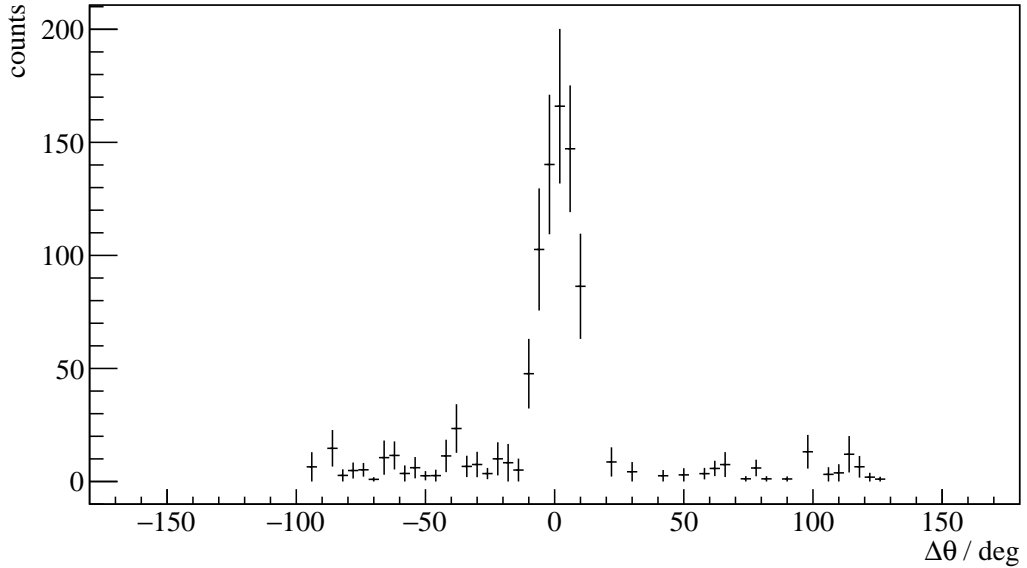


**Figure 3.14:** Polar angle difference  $\Delta\theta$  between two uncorrelated photons of the  $\pi^0\eta$  final state.

Considering the above one can now say that  $2\pi^0$  and  $\pi^0\eta$  events pass the  $\eta'$  event selection because

1. two uncorrelated low energy photons are lost during reconstruction and the remaining two pass the kinematic cuts by chance, since they too are uncorrelated (see figure 3.15a),
2. one low energy photon is lost. Two uncorrelated of the remaining three photons are combined to one in favor of the higher energetic photon since they were emitted in the same direction. The two reconstructed photons are uncorrelated and pass the event selection randomly, as shown in figure 3.15b.

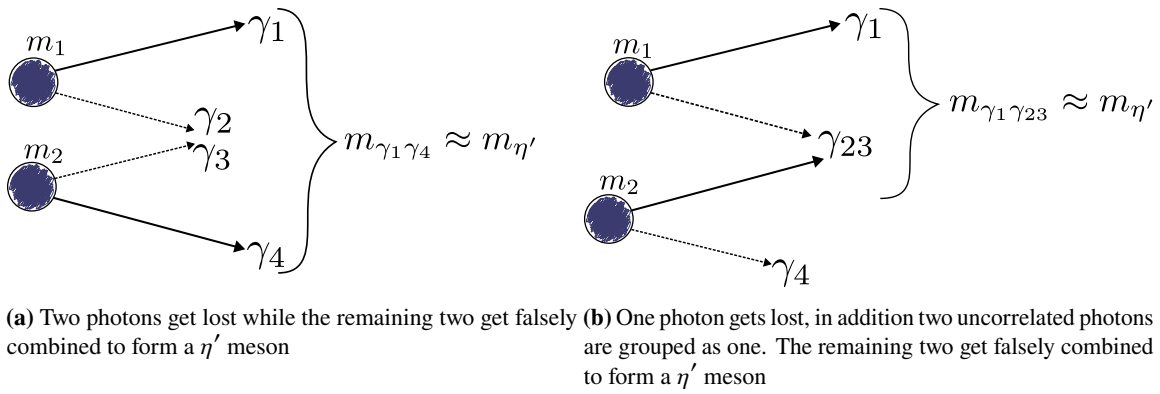


**Figure 3.15:** Illustration of the misidentification process during reconstruction

These claims are indeed further validated if one examines the polar angle that is reconstructed from the falsely assigned  $\eta'$  candidates using the surviving two photon momenta. This can be compared to the generated polar angle that is built using all four final state photon momenta in the CMS  $\mathbf{p}_{\gamma_i}$ . They add up to the artificial two-meson momentum  $\mathbf{p}_m$  which in the CMS has the same magnitude but opposite direction as the recoil proton with momentum  $\mathbf{p}_{\text{recoil}}$

$$\mathbf{p}_m = \sum_{i=1}^4 \mathbf{p}_{\gamma_i} = -\mathbf{p}_{\text{recoil}}.$$

If the lost photons have very low energies and/or are emitted in the same direction as other photons one would expect the polar angle that is spanned by the four final state photons approximately agrees with the polar angle that is built using the two photons that survived event selection, such that  $\cos \theta(4\gamma) \approx \cos \theta(2\gamma)$ . This is exactly what is observed, as figure 3.16 shows for both background reactions: the generated CMS angle  $\cos \theta_{\text{gen.}}$  is plotted against the reconstructed CMS angle  $\cos \theta_{\text{rec.}}$ . The events are clearly distributed around the slope  $\cos \theta_{\text{gen.}} = \cos \theta_{\text{rec.}}$  which is indicated by the solid line. This is an important result for the later analysis: if the background contributions are taken into account quantitatively then the extracted beam asymmetry has to be corrected by the asymmetry stemming from background reactions. This is only possible if the background reactions from e.g.  $2\pi^0$  events realize the same bins in beam energy and CMS angle as in a dedicated measurement of the beam asymmetry in the respective photoproduction reaction.

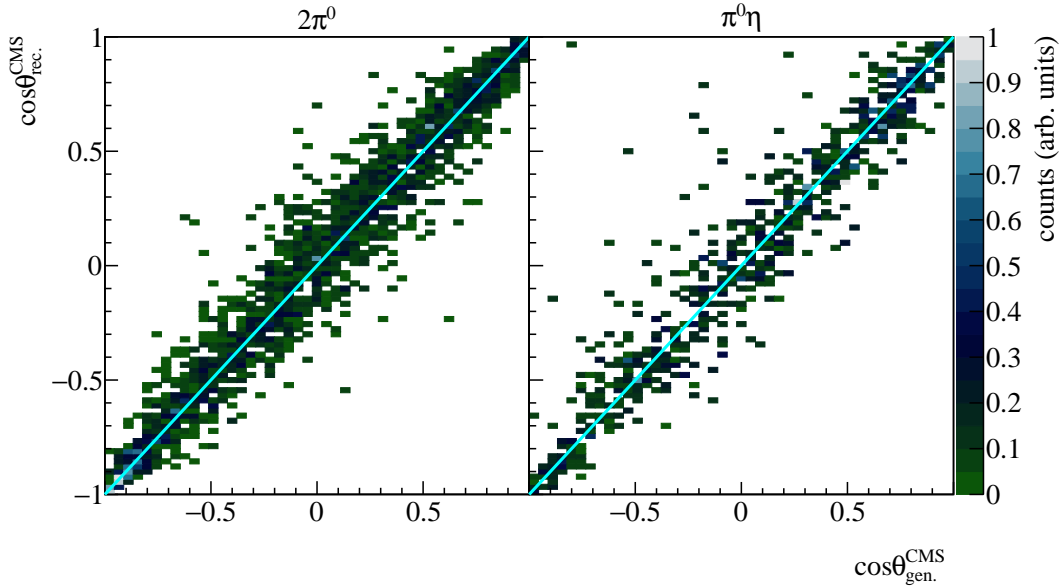


**Figure 3.16:** Generated CMS angle  $\cos\theta_{\text{gen}}$  vs. reconstructed CMS angle  $\cos\theta_{\text{rec}}$  for both background reactions. The slope  $\cos\theta_{\text{gen}} = \cos\theta_{\text{rec}}$  is indicated by the solid line.

### 3.4.3 Examination of additional cuts

Since the background contributions are significantly beyond a negligible amount it would be desirable to remove them through additional cuts that at the same time do not remove too many signal events. However, this proved to be a complicated task because the background reactions are reconstructed from real photons which happen to be in the  $\eta'$  invariant mass range. Therefore they are not distinguishable from  $\eta' \rightarrow \gamma\gamma$  photons in terms of energy, momentum (direction) or created cluster size in the calorimeter crystals. The combination of two photons into one also is not observable as such since the impact of one photon with energy  $E$  may create a cluster with cluster size  $C$  which at the same time can be created by two photons in the same direction with energies  $E_1 + E_2 = E$  and cluster sizes  $C_1 + C_2 = C$ . Thus, to find any characteristics that separate background from signal events, one has to analyze properties of either the recoil proton or the reaction kinematics as a whole.

#### Proton cut

Very close to the  $\eta'$  production threshold, the meson system is not boosted very much in forward direction as long as real  $\eta'$  mesons are produced. As a consequence the recoil proton may escape to very forward angles in the lab system which corresponds to the proton being detected in the MiniTAPS calorimeter. Falsely reconstructed  $2\pi^0$  or  $\pi^0\eta$  events have lower production thresholds such that the mesons will be boosted forward and the recoil proton is detected rather in the forward detector or the Crystal Barrel calorimeter. Figure 3.17 shows for the first two energy bins (starting at 1400 MeV) the detector that was hit by the recoil proton for  $\eta'$ ,  $2\pi^0$  and  $\pi^0\eta$  MC data. At threshold nearly all protons of  $\eta'$  events are detected in the MiniTAPS calorimeter while this is only the case for 57% of  $2\pi^0$  events and 20% of  $\pi^0\eta$  events. Towards higher energies this distribution along detectors smears out

and is approximately equal for all reactions. Yet, not enough statistics are collected in the energy bin close to threshold for a cut based on the proton detector hit to have significance, as this bin contains less than 7% of total  $\eta'$  candidates. The poor statistics in this bin also make determining background from MC fits difficult. Thus, as has been mentioned before, the energy bin from 1 400 to 1 500 MeV was not included in the analysis. Consequently no cut based on proton detector hits could be applied to the remaining data. Apart from directional information near threshold protons from signal and background events could not be distinguished.

### Reaction kinematics

As has been mentioned before, the measured photoproduction reactions are in fact overdetermined, meaning that one reaction particle can be treated as missing. This can be used to calculate the beam photon energy

$$E_{\gamma}^{\text{calc}} = \frac{-0.5 \cdot m_{\eta'}^2 + m_p E_{\eta'}}{m_p - E_{\eta'} + |p_z|_{\eta'}}, \quad (3.11)$$

where  $m_p$  is the proton mass,  $m_{\eta'}$  the  $\eta'$  mass,  $E_{\eta'}$  is the meson energy and  $|p_z|_{\eta'}$  is the meson momentum in  $z$ -direction. Comparing this with the measured beam energy one may tell  $\eta'$  events apart from background events where mesons with smaller masses have been produced. If equation (3.11) is used to calculate the beam energy, i.e. inserting the  $\eta'$  mass, background events from reactions with smaller masses will cause smaller calculated beam energies. The difference of measured and calculated beam energy  $E_{\gamma}^{\text{meas}} - E_{\gamma}^{\text{calc}}$  is shown in figure 3.18. The data points are shown as open circles and solid histograms represent fitted MC data where the turquoise histogram is the sum of all MC histograms. A broad peak centred slightly off 0 towards lower energy differences is visible. It also exhibits a broad shoulder towards higher energy differences. The MC describe the data very well, consisting mainly of  $\eta'$  and  $2\pi^0$  MC, as expected. The  $2\pi^0$  MC show a trend towards energy differences  $> 0$ , as predicted by equation (3.11). In principle the distribution of  $2\pi^0$  and  $\eta'$  MC now allow to introduce an upper bound on the beam energy difference rejecting any desired amount of  $2\pi^0$  background. However, simultaneously a significant amount of  $\eta'$  events have to be discarded if this cut should have remarkable influence on the  $2\pi^0$  events, as is shown in table ???. Considering that only 8000  $\eta'$  candidates could be extracted, any cut removing sizable fractions of signal events will have grave impact regarding the statistical error for the later analysis of the beam asymmetry. It was decided not to imply any further cuts on the data and proceed with the selected events as described previously. Because results for the beam asymmetry in  $2\pi^0$  and  $\pi^0\eta$  production are available [CITE\(P. Mahlberg, Georg Urff?\)](#) it is not crucial to remove all remaining background as the extracted beam asymmetry can be corrected proportionately, depending on the amount and type of background in a particular bin.



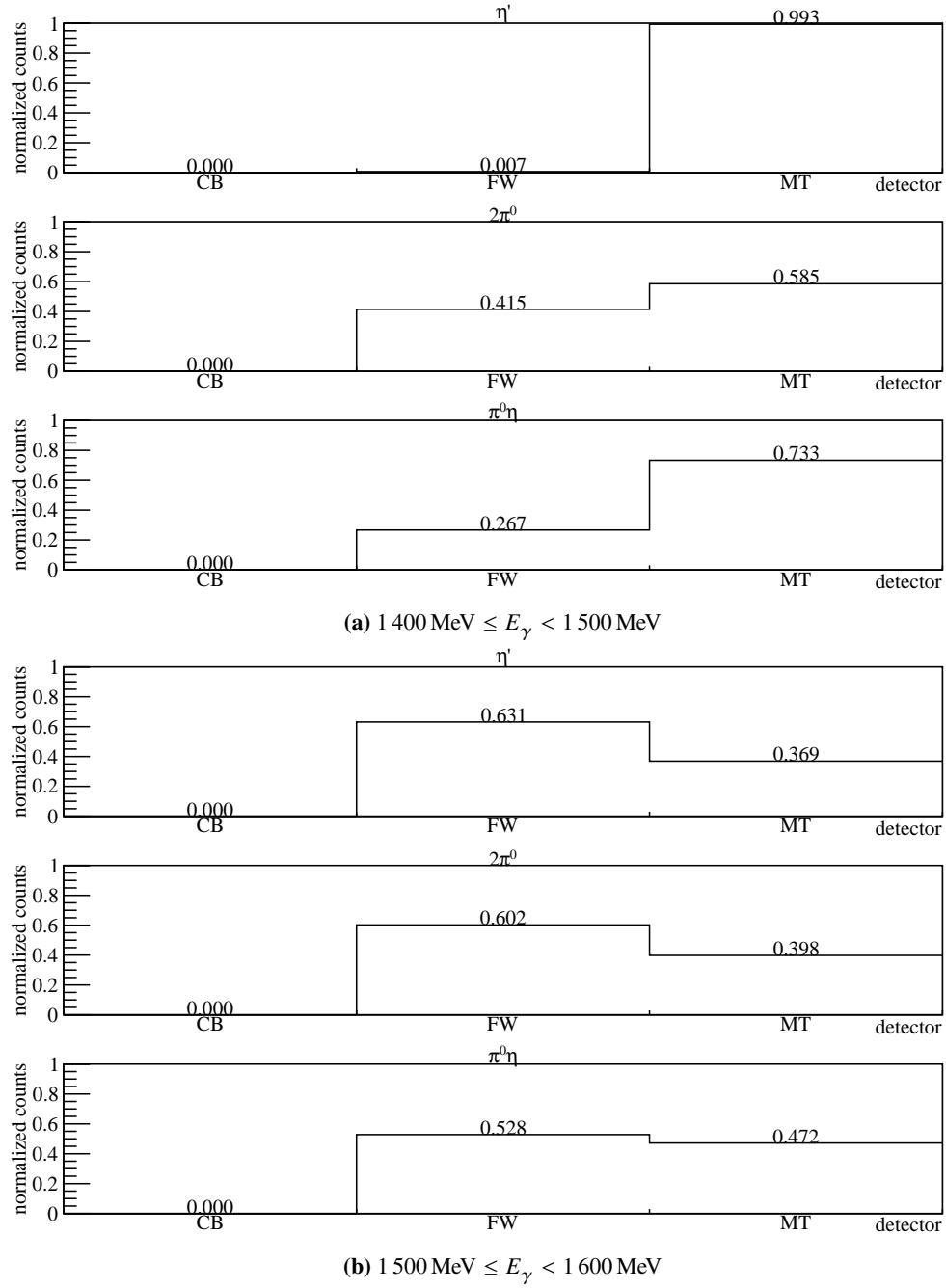


**Figure 3.17:** Detector hits of the recoil proton, as obtained from MC data for the production of  $\eta'$ ,  $2\pi^0$  and  $\pi^0\eta$ . CB: Crystal Barrel, FW: forward detector, MT: MiniTAPS

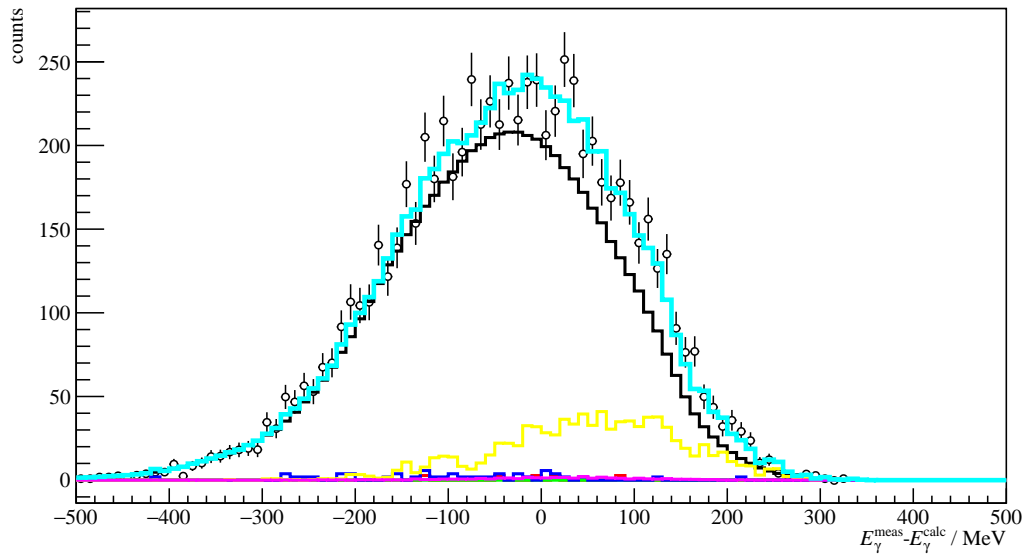


**Figure 3.18:** Difference in measured and calculated beam energy. Data points are shown as open circles, MC data as solid histograms: in black  $\eta'$ , in green  $\pi^0$ , in red  $\eta$ , in blue  $\omega$ , in yellow  $2\pi^0$  and in magenta  $\pi^0\eta$ . The turquoise histogram is the sum of all MC histograms.



# Bibliography

---

- [Afz22] F. Afzal, *Private communication*, 2022 (cit. on p. 11).
- [Zyl+20] P. Zyla et al., *Review of Particle Physics*, PTEP **2020** (2020) 083C01 (cit. on pp. 11, 15, 17).
- [Afz19] F. N. Afzal, *Measurement of the beam and helicity asymmetries in the reactions  $\gamma p \rightarrow p\pi^0$  and  $\gamma p \rightarrow p\eta$* , PhD thesis: Rheinische Friedrich-Wilhelms-Universität Bonn, 2019, URL: <https://hdl.handle.net/20.500.11811/8064> (cit. on pp. 11, 20, 21).
- [Ike+00] H. Ikeda et al., *A detailed test of the CsI(Tl) calorimeter for BELLE with photon beams of energy between 20-MeV and 5.4-GeV*, Nucl. Instrum. Meth. A **441** (2000) 401 (cit. on pp. 17, 19).
- [Cre+09] V. Crede et al., *Photoproduction of eta and eta-prime mesons off protons*, Phys. Rev. C **80** (2009) 055202, arXiv: 0909.1248 [nucl-ex] (cit. on p. 23).
- [Die+20] M. Dieterle et al., *Helicity-Dependent Cross Sections for the Photoproduction of  $\pi^0$  Pairs from Nucleons*, Physical Review Letters **125** (2020), URL: <https://doi.org/10.1103/PhysRevLett.125.062001> (cit. on p. 23).
- [Käs+18] A. Käser et al., *First measurement of helicity-dependent cross sections in  $\pi^0\eta$  photoproduction from quasi-free nucleons*, Physics Letters B **786** (2018) 305, URL: <https://doi.org/10.1016/j.physletb.2018.10.006> (cit. on p. 23).



# List of Figures

---

1.1	Running coupling of QCD. The colored data points represent different methods to obtain a value for $\alpha_s$ . For more details it may be referred to [Zyl+20]. . . . .	2
1.2	Calculated nucleon (isospin $I = 1/2$ ) resonances compared to measurements. Left in each column are the calculations [ <b>bonnmodel</b> ], the middle shows the measurements and PDG rating [Zyl+20] . . . . .	3
1.3	FEYNMAN diagram for the s-channel photoproduction of pseudoscalar mesons, adapted from [Afz19] . . . . .	4
2.1	[ <b>cb</b> ] . . . . .	7
2.2	[ <b>cb</b> ] . . . . .	8
2.3	[ <b>cb</b> ] . . . . .	8
2.4	D. WALTHER in [ <b>urban</b> ] . . . . .	9
2.5	[ <b>cb</b> ] . . . . .	9
2.6	[ <b>cb</b> ] . . . . .	10
3.1	Distribution of event classes in $\eta' \rightarrow \gamma\gamma$ production . . . . .	12
3.2	Time information of all final state particles and the beam photon for 3PED $\eta'$ production	13
3.3	Reaction time $t_r$ for 3PED $\eta'$ production . . . . .	14
3.4	Coplanarity of the $p\eta'$ final state with all other cuts applied for the energy bin $1\,500\,\text{MeV} \leq E_\gamma < 1\,600\,\text{MeV}$ . The vertical dashed lines show the cut ranges obtained from a gaussian fit to the data (open circles). The solid black histograms represent fitted MC data of $\eta' \rightarrow \gamma\gamma$ . . . . .	18
3.5	Polar angle difference of the $p\eta'$ final state with all other cuts applied for the energy bin $1\,500\,\text{MeV} \leq E_\gamma < 1\,600\,\text{MeV}$ . The vertical dashed lines show the cut ranges obtained from a gaussian fit to the data (open circles). The solid black histograms represent fitted MC data of $\eta' \rightarrow \gamma\gamma$ . . . . .	18
3.6	Missing mass of the $p\eta'$ final state with all other cuts applied for the energy bin $1\,500\,\text{MeV} \leq E_\gamma < 1\,600\,\text{MeV}$ . The vertical dashed lines show the cut ranges obtained from a fit to data (open circles) employing a NovosIBIRSK function. The solid colored histograms represent fitted MC data from relevant photoproduction reactions: in black $\eta'$ , in green $\pi^0$ , in red $\eta$ , in blue $\omega$ , in yellow $2\pi^0$ , magenta $\pi^0\eta$ . The turquoise histogram is the sum of all MC histograms. . . . .	19

3.7	Invariant mass of the $p\eta'$ final state with all other cuts applied for all energy and angular bins. The open circles represent the measured data, the solid colored histograms fitted MC data from relevant photoproduction reactions: in black $\eta'$ , in green $\pi^0$ , in red $\eta$ , in blue $\omega$ , in yellow $2\pi^0$ and in magenta $\pi^0\eta$ . The turquoise histogram is the sum of all MC histograms. . . . .	20
3.8	Invariant mass of the $p\eta'$ final state with all other cuts applied for the energy bin $1\,500\text{ MeV} \leq E_\gamma < 1\,600\text{ MeV}$ . The vertical dashed lines show the cut ranges obtained from a gaussian fit to the $\eta'$ MC data (solid black histogram). The open circles represent the measured data, the solid colored histograms fitted MC data from relevant photoproduction reactions: in black $\eta'$ , in green $\pi^0$ , in red $\eta$ , in blue $\omega$ , in yellow $2\pi^0$ and in magenta $\pi^0\eta$ . The turquoise histogram is the sum of all MC histograms. . . . .	21
3.9	Acceptance for the reaction $\gamma p \rightarrow p\eta'$ after all cuts that have been discussed so far for 2.5PED and 3PED events . . . . .	22
3.10	Fraction of background events in the analyzed beam energy and angular bins. . . . .	23
3.11	Acceptance for possible background contributions . . . . .	24
3.12	Generated energies of the two lowest energy photons in $2\pi^0$ photoproduction MC data. The threshold of 20 MeV is marked by a vertical red line. Lowest energy photon is shown on the top, second lowest energy photon is shown on the bottom. . . . .	25
3.13	Generated energies of the two lowest energy photons in $2\pi^0$ and $\pi^0\eta$ photoproduction MC data. The threshold of 20 MeV is marked by a vertical red line. Lowest energy photon is shown on the top, second lowest energy photon is shown on the bottom. . . . .	26
3.14	Polar angle difference $\Delta\theta$ between two uncorrelated photons of the $\pi^0\eta$ final state. . . . .	26
3.15	Illustration of the misidentification process during reconstruction . . . . .	27
3.16	Generated CMS angle $\cos\theta_{\text{gen.}}$ vs. reconstructed CMS angle $\cos\theta_{\text{rec.}}$ for both background reactions. The slope $\cos\theta_{\text{gen.}} = \cos\theta_{\text{rec.}}$ is indicated by the solid line. . . . .	28
3.17	Detector hits of the recoil proton, as obtained from MC data for the production of $\eta'$ , $2\pi^0$ and $\pi^0\eta$ . CB: Crystal Barrel, FW: forward dector, MT: MiniTAPS . . . . .	30
3.18	Difference in measured and calculated beam energy. Data points are shown as open circles, MC data as solid histograms: in black $\eta'$ , in green $\pi^0$ , in red $\eta$ , in blue $\omega$ , in yellow $2\pi^0$ and in magenta $\pi^0\eta$ . The turquoise histogram is the sum of all MC histograms. . . . .	31

# List of Tables

---

1.1	Summary of the particles of the SM . . . . .	1
1.2	Allowed quantum numbers for the intermediate resonance state $N^*/\Delta^*$ . . . . .	4
3.1	The five most probable decay modes of the $\eta'$ meson. The most probable further decay with according branching ratio is shown in brackets.[Zyl+20] . . . . .	11
3.2	Examined MC reactions that were used in sum for the fit . . . . .	16
3.3	Fit functions and cut ranges for each variable . . . . .	17
3.4	Total cross sections $\sigma$ in the energy range 1 500 to 1 800 MeV, branching ratios (BR) to $n\gamma$ final states and maximum acceptance $\tilde{A}$ for signal and possible background contributions . . . . .	23